Magneto-optical fibre sensors for electrical industry: analysis of performances

S. Donati
V. Annovazzi-Lodi
T. Tambosso

Indexing terms: Optical fibres, Optoelectronics

Abstract: We present an analysis of all-fibre sensors intended for current and magnetic field measurements in electrical systems. After reviewing magneto-optic effects in connection to application requirements, we calculate the theoretical performances of the sensor, in terms of sensitivity, bandwidth, dynamic range and linearity, both for polarimetric and interferometric readout schemes. Sources of errors in the fibre and optical components are analysed, and their limitations to sensitivity are evaluated. Birefringence control is discussed, and the results applied to develop several linked and unlinked sensor configurations. Finally, experimental data are compared to theoretical values.

1 Introduction

In power systems applications, fibre optic sensors attract considerable interest in view of the well known characteristics of passive structure, intrinsic insulation, non-invasiveness and improved performances (especially bandwidth) in respect to conventional devices [1, 2]. To date, a number of fibre optic sensors have been shown to be feasible, either as fixed-installation replacements of existing devices or as probes for special-purpose instruments [3–7]. Reported examples fall into these classes:

(*a*) current and voltage sensors aimed to replace CT and VT transformers on HV lines, or to perform special measurements (such as direct current measurements, and high frequency transient measurement).

(*b*) Magnetic field and electric field sensors for measuring stray flux in electrical machinery and insulators.

(*c*) Temperature sensors to probe internal overheating of transformers and generators.

(*d*) Wind speed and stress sensors to monitor long-haul conductor lines.

For application in power systems, several requirements and specifications must be met, and these have a direct impact on permissible sensor design. The requirements of minimum size, electrical passive structure and non-invasiveness are common to fixed and mobile units. As a consequence, conductive elements are not allowed in the sensing region, the line current cannot be shunted through the sensor, and the distributions of electrostatic and magnetic fields are substantially unaltered by the sensor.

Paper 6148J (E13), received 21st December 1987

The authors are with the Department of Electronics, University of Pavia, Via Abbitegrasso 209, 27100 Pavia, Italy

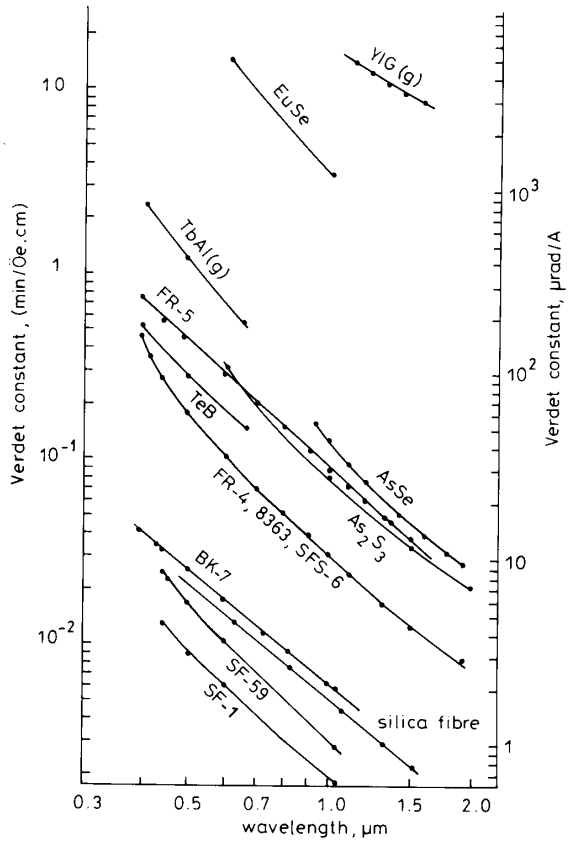

Fig. 1 *Verdet constant of some glasses and garnets* (g)

Both AC (single and 3-phase) and DC current sensors are of interest. In fixed installations, linkage to the line is permitted, and the performance specifications of the sensor, e.g. a measurement range $1 \div 10000$ A with 1% accuracy and 0.1 s response time, are those of conventional CT s used in power management; a larger bandwidth (100 kHz) with reduced accuracy (5%) is required for fault and transient diagnostics. The sensor can withstand HV voltages, and can operate in the field conditions with a lifetime of 10 years [2]. In mobile applications, intended for inspection and maintenance, the sensor is unlinked to allow operation without line disconnection, and has the same specifications as above, except for lifetime and accuracy (5%).

Magnetic field sensors, aimed to diagnostics of large power machinery, have less standard specifications. However, the typical range is $0.01 \div 1000$ gauss, with 5%

accuracy at mains frequency and operating temperature of $0 \div 120°C$.

In this paper, we will deal with current and magnetic field sensors based on the Faraday effect, and implemented with the all-fibre technology.

While the micro-optic technology is close to meet in the field the above specifications for current sensors [3, 5], the all-fibre technology has the advantage of simpler and more rugged design of the sensing element, offers flexibility in sensor geometry, and lends itself more easily to distributed-type sensors.

2 Magneto-optical transduction effects

Several well known magneto-optical effects [8–13] can be envisaged for the direct transduction of magnetic field or current into an optical measurand. These are:

(*a*) Zeeman effects (longitudinal and transverse).

(*b*) Faraday effect (or longitudinal Zeeman-inverse effect).

(*c*) Voigt effect (or transverse Zeeman-inverse effect).

(*d*) Cotton-Mouton effect (magnetic counterpart of electro-optical Kerr effect).

(*e*) Magneto-optical Kerr effect (reflection anisotropy).

(*f*) Magnetic dichroism (absorption anisotropy).

In addition, an efficient transduction can be obtained through two-step *indirect* effects. Reported examples [6, 14] are:

(*g*) Magnetostriction combined to elasto-optic conversion.

(*h*) Joule dissipation followed by thermal expansion.

The Faraday effect was the first magneto-optical effect to be proposed and demonstrated in fibre current sensors [1] and still is the most viable approach because of the substantial Verdet constant V that is available in several glasses [8] and in ordinary fibres. The Verdet constant relates the line integral of the magnetic field strength H to the rotation Φ of the polarisation plane of a linearly polarised wave propagating along the line L:

$$\Phi = V \int_L \underline{H} \cdot \underline{dl} \tag{1}$$

Equivalently, Φ is the nonreciprocal phaseshift for circularly polarised waves. Φ is positive if the polarisation is right handed, and negative if the polarisation is left handed.

From a model based on the classical atomic dipole oscillator [9, 12] an expression for the Verdet constant is found [12] in terms of optical constants and of the number N of dipole oscillators. By rearranging this expression to eliminate N, we obtain:

$$V = \frac{e\mu}{mc} \frac{n^2}{2n} \frac{\lambda_0^2}{\lambda^2 - \lambda_0^2} \tag{2}$$

where λ_0 is the wavelength of the absorption resonance, μ is the permeability which can be assumed to be equal to μ_0 at optical frequencies [11], and $e\mu_0/mc = 741\ \mu r/A$ is the Bohr magneton. Eqn. 2 correctly predicts the λ^{-2} trend for $\lambda \gg \lambda_0$, which is evident in Fig. 1, as well as the dependence on n of V. For pure amorphous silica, with $\lambda_0 = 0.118\ \mu m$ [15], $V = 5.54\ \mu r/A$ at $\lambda = 850$ nm for AsS_3, $V = 63\ \mu r/A$ at $\lambda = 850$ nm.

In eqn. 1, the integration path, set by the fibre geometry, determines the measurand that is fundamentally transduced in the angle Φ. Open path fibres (Figs. 2*a* and *b*) are basically *magnetic field* sensors, since they perform a sort of averaging of H on the measure path. The current I is also indirectly measured, but with a scale factor dependent on the geometry. Closed-path fibres (Figs. 2*c* and *d*) actually perform a closed-line integral of H, and the result is, irrespective of the geometry:

$$\Phi = VNI \qquad \text{(linked coil)} \tag{3}$$

$$\Phi = 0 \qquad \text{(unlinked coil)} \tag{3'}$$

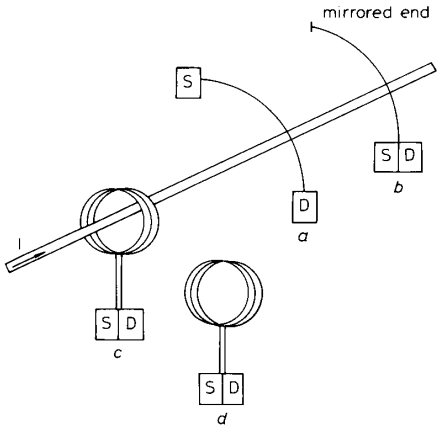

Fig. 2 *Geometries of magnetic field and current sensors*
S = source
D = detector

where N is the number of turns. These are therefore true current sensors, giving a rotation Φ dependent only on the current I carried by the wire and on the number of linked turns N, while the sensitivity to external field or unlinked current is zero. Strictly, the above applies to a fibre with negligible linear birefringence; compounding and quenching effects are treated in Section 4.

The Voigt effect is consequent to the transverse Zeeman effect, exactly like the Faraday effect is consequent to the longitudinal [11]. With a transverse magnetic field H_T applied to a fibre, a birefringence is induced between perpendicular and parallel linearly-polarised waves, and the corresponding phaseshift $\Phi = \Delta nkl$ is

$$\Phi = V_q \int_L H_T^2\, dl \tag{4}$$

where, for simplicity, a constant magnetic field direction has been assumed.

From an analysis based on classical dipole theory, the Voigt constant V_q can be evaluated as:

$$V_q = \frac{n\lambda}{\pi(n^2 - 1)} V^2 \tag{5}$$

where V is the Verdet constant given by eqn. 2. Since the Voigt phaseshift Φ is quadratic in the magnetic field component H_T, it is order of magnitudes smaller than the Faraday phase Φ. Although this conclusion rules out the application of the Voigt effect to current sensing, it justifies *a-posteriori* the correctness of eqn. 1 even for large amplitudes of transverse H_T components.

For the application in all-fibre sensing, the Zeeman effect shall also be considered since rare-earth doped fibre-lasers have been developed [16]. It is well known that the normal Zeeman effect is observed as the splitting of the atomic line either into two circularly or linearly polarised lines, whether the magnetic field is parallel or perpendicular to the light vector. The frequency splitting

Δv is given by [8–10]:

$$\Delta v = \frac{e}{m}\frac{\mu_0}{4\pi} H = ZH \tag{6}$$

where

$$Z = 17.6 \text{ kHz/(A/m)} = 1.4 \text{ MHz/Oe.} \tag{7}$$

Several conceptual configurations can be devised to develop a Zeeman-effect fibre sensor, both passive and active. For example, Δv can be read as the shift in absorbance peaks relative to two orthogonal polarised waves launched in the fibre (linear for a transverse magnetic field and circular for a longitudinal field). Or, the fibre itself provided with mirror splices can be pumped to oscillate, as in a Zeeman gas laser [17], on two orthogonal modes the frequency difference of which gives Δv, albeit reduced by a factor $\eta \ll 1$ owing to the frequency pulling effect [17]. In any case, unlike the Faraday effect sensor, the current measurement would have a geometry-dependent scale factor. Also, serious problems arise from the large atomic linewidth of the doped fibre, and because of the intermixing of longitudinal and transverse effects altering the polarisation state when the magnetic field has both a parallel and a perpendicular component. As a result, a Zeeman-effect sensor seems presently still far from achieving a potential sensitivity comparable to that of the Faraday effect.

The counterpart of the electro-optic Kerr effect, the Cotton-Mouton magneto-optic effect is identical to the Voigt effect from a phenomenological point of view, but it is owing to the orientation of anisotropic molecules which yields apparent values of V_q much larger than those supplied (eqn. 5) by the electron moment, yet too small (at least, in known materials) [8] for current sensing.

The Kerr-reflection effect concerns the change of polarisation state upon reflection on a magnetic surface, from linear to rotated elliptical in general. According to the direction of the magnetisation vector $\underline{M}$ in respect to the surface $\underline{n}_s$ and incident plane $\underline{n}_i$ normals, the effect is defined as polar ($\underline{M}//\underline{n}_s$), longitudinal ($\underline{M}\perp\underline{n}_s$, $\underline{n}_i$) or transverse ($\underline{M}\perp\underline{n}_s$, $\underline{M}//\underline{n}_i$) [8]. All three effects are small (min of arc for kOe) except for ferromagnetic materials at saturation. Although adequate for the readout of magneto-optic disk memories and for the measurement of the thin film thickness on magnetic heads [18], the Kerr reflection coefficient is too small to hint the noncontact measurement in reflection on a conductor line.

Lastly, magnetic dichroism is exhibited by some ferrimagnetic materials [13] at low temperatures and near to the absorption lines, as an anisotropy of the attenuation coefficient, with respect to right- and left-handed circular polarisations. A simple differential-intensity scheme can read the magnetic dichroism induced by a current or a magnetic field, however no material is known for room temperature application [13].

Among indirect transduction effects, magnetostriction combined to an elasto-optic element is well established for building a magnetometer [6]. A nickel jacket is used as the magnetostrictive element to impress a longitudinal stress T_1 on the fibre, that acts as the elasto-optic element, and converts the stress in a pathlength variation:

$$\Delta\Phi/\Phi = q_1 T_1,$$

where q_1 is related to the elasto-optic matrix elements q_{ij}, and $\Phi = nkl$ is the optical pathlength. To circumvent the quadratic response of the magnetostrictive effect, giving $T_1 = m_T H^2$, a bias AC magnetic field $H_0 \sin \omega_0 t$ is superimposed to the measurand field h by means of a winding on the sensing fibre; thus, the stress, and hence the phase $\Delta\Phi$, have a component $2hH_0 \sin \omega_0 t$ at the bias frequency, which is linearly related to the measurand magnetic field h. In power systems, the bias winding and the highly conductive nickel jacket violate the requirements of passive electrical structure and inherent insulation of the sensor. However, this problem is solved if a magnetic glass or a hard-ferrite of permanent magnet-grade are used as the magnetostrictive coating, to ensure both a high resistivity and an adequate coercitive force H_c providing a constant bias field. Hence, the sensor becomes sensitive to AC magnetic fields $h = h_0 \sin \omega t$, external or produced by line current, yielding a phase:

$$\Delta\Phi = 2hH_c \sin \omega t$$

Because of the anisotropy of magnetisation, the sensor is sensitive only to the longitudinal magnetic field component, and eqns. 1 and 3 apply formally by letting:

$$V = (4\pi/\lambda) q_1 m_T H_c$$

where Φ is interpreted as the excess phaseshift owing to the current I. Joule-heating, followed by thermal expansion, has been proposed as an indirect transduction effect for current measurements [14]. This invasive method requires the shunting of the measurand current in the sensor. Also, bandwidth appears to be limited by the long thermal constant of the resistive coating of the fibre, thus reducing the interest of this approach for power system applications [14].

3 Optical readout schemes

In this Section we analyse polarimetric and interferometric readout schemes of the Faraday rotation phase Φ, to assess performances of the fibre sensor in terms of noise, bandwidth, linearity and dynamic range. The analysis is referred here to current sensing and in Section 4 it will be extended to magnetic field sensing.

3.1 Polarimetric readout

In the basic scheme [2, 19, 20] of polarimetric readout (see Fig. 3), a linearly polarised wave is launched in the

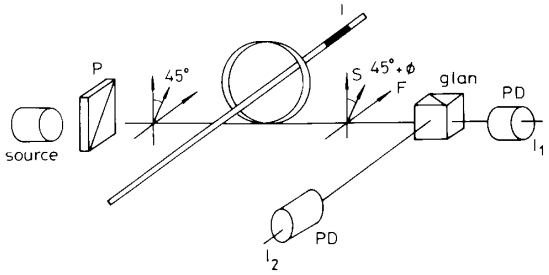

Fig. 3 *Basic polarimetric readout of Faraday rotation* Φ

fibre and the output is analysed by a polarisation beam-splitter (e.g. a Glan cube) with the principal axes oriented at 45° with respect to the input. Thus, two signals I_1 and I_2 are supplied by the photodectors:

$$I_1 = I_0 \cos^2(45° + \Phi) \tag{8}$$

$$I_2 = I_0 \sin^2(45° + \Phi) \tag{9}$$

To obtain a signal dependent only on Φ, regardless of the photodetected current I_0 and associated fluctuations due to optical power, launching efficiency and detector responsivity [20], the signal S is computed as the ratio of the difference to the sum of I_1 and I_2:

$$S = (I_1 - I_2)/(I_1 + I_2) = \sin 2\Phi \tag{10}$$

Excluding fibre-related errors, let us consider the minimum detectable signal S. Noise contributions to S are: shot noise of detected currents I_1 and I_2, Johnson noises of photodetector preamplifiers and excess noise of the source. A calculation of the variance $\sigma^2(S) = \langle (S - \langle S \rangle)^2 \rangle$ associated with the signal S gives as a result, for $\sigma(S) \ll \langle S \rangle$:

$$\sigma^2(S) = (2eB/I_0)[F + 4kT/eRI_0](1 + S^2) \tag{11}$$

where e is electronic charge, $kT/e = 26$ mV, B is the measurement bandwidth, R is the equivalent noise resistance of the preamplifier, and F is an excess noise factor. For $RI_0 \gg 4kT/e \simeq 104$ mV, the Johnson noise is negligible, and the quantum noise limit $2eB/I_0$ of the photodetected current is reached. The corresponding noise-equivalent

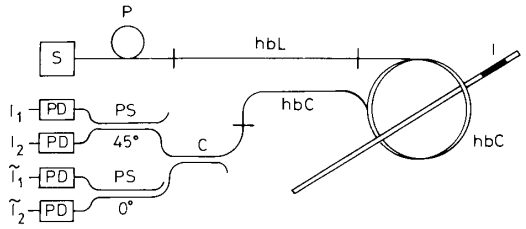

Fig. 4 *All-fibre polarimetric readout*

P = polariser
hbL = high linear-birefringence fibre
hbC = high circular-birefringence fibre (or twisted spun)
C = coupler (nonpolarising)
PS = polarisation selective splitters, oriented at 0° and 45°
PD = photodetector
(|) = splices or connectors

current $\sigma(I)$ at the quantum noise limit is obtained, by random variable transformation, as

$$\sigma(I) = \sigma(S)/|\, dS/dI \,|$$

where $dS/dI = (dS/d\Phi)(d\Phi/dI)$ is computed from eqns. 3 and 10 with the result:

$$\sigma(I) = (1/2VN)(2eB/I_0)^{1/2} \tag{12}$$

In Fig. 5, $\sigma(I)$ is plotted against bandwidth B with the detected current I_0 as a parameter, for $V = 2.5$ μr/A (ordinary silica fibres) and number of turns $N = 50$.

Also shown in Fig. 5 is the angle $2\Phi(\sigma) = 2VN\sigma(I)$ corresponding to $\sigma(I)$, that can also be interpreted as the noise-to-signal ratio N/S required in detecting I_1 and I_2, since $2\Phi(\sigma) = \sigma(I_0)/I_0$, or as the smallest signal S_σ to be resolved in the handling circuits, since $S_\sigma = 2\Phi(\sigma)$ from eqn. 10.

In regard to the excess noise factor F, excluding fibre-related effects, the main contributions come from excess white noise of the source and $1/f$ noises of source and photodetector. Above $1/f$ corner frequency, it is well known that LEDs are quiet sources, with F rarely exceeding a few tenths of a decibel. Both monomode and multimode diode lasers exhibit, near threshold, a peak of excess noise (with F up to 20 dB) levelling off above threshold. Superluminescent LEDs are the most noisy, with $F = 0.5 \div 10$ dB on all their operating current range [22].

The bandwidth B of the current sensor is limited intrinsically by material relaxation time τ_r and by transit time effects in the sensing coil. Also, one must consider

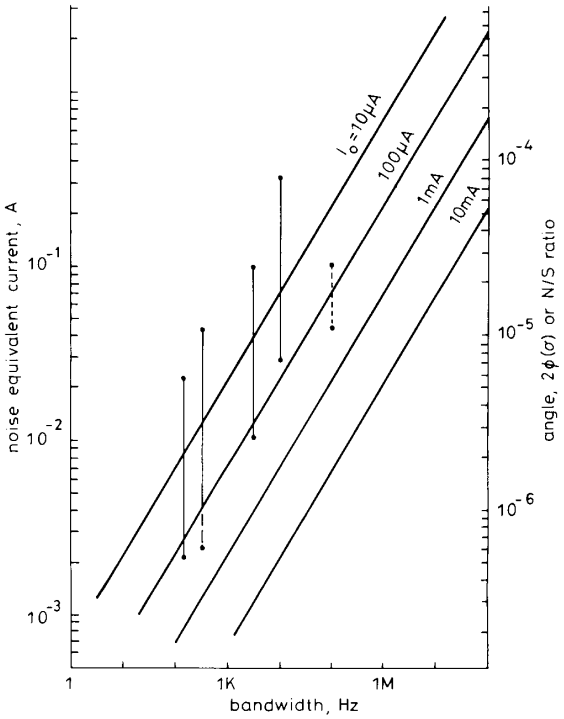

Fig. 5 *Noise equivalent current $\sigma(I)$ of current sensor at quantum limit against bandwidth, and with detected current I_0 as parameter*

Also shown is the rotation $2\Phi(\sigma)$ corresponding to $\sigma(I)$, or noise-to-signal ratio of the measurement
Vertical bars are experimental data
Assumed parameters: $N = 50$; $V = 2.5$ μrad/A

the extrinsic limitation due to the frequency response of the photodetector and associated circuits. In diamagnetic materials, the relaxation time constants of the Faraday effect fall in the sub-nanoseconds range [9] and can therefore be ignored.

Denoting the transit time in the coil of N turns of radius r by $\tau(=2\pi nNr/c)$, the time domain response to a $1(t)$ step of current is

$$\begin{aligned} \Phi &= 0 & t &\leqslant 0 \\ &= \Phi_0 t/\tau & 0 &\leqslant t \leqslant \tau \\ &= \Phi_0 & t &> \tau \end{aligned}$$

Hence, the δ-impulse response of the coil is a rectangular pulse of time duration τ; neglecting an unessential delay, the transfer function is then

$$F(\omega) = \sin(\omega\tau/2)/(\omega\tau/2)$$

and by calculating the -3 dB point of $F(\omega)$, one has for the bandwidth B:

$$B(3\text{ dB}) = 0.44/\tau = 0.44c/2\pi nNr \tag{13}$$

This bandwidth is relatively high, e.g. for a coil radius $r = 1$ cm and $N = 50$, $n = 1.5$, we have $B = 28$ MHz.

Commonly, electronic filtering is used to improve sensitivity at the expense of bandwidth. However, if the maximum bandwidth is desired, the photodetector may become the limiting factor. State of the art design of J-FET preamplifiers [21] with *pin* silicon photodiodes yields a typical resistance-bandwidth product

$RB = 0.8 \div 1.5$ (MΩ MHz) with nearly Johnson-noise limited performance in the range of resistances R = 5K ÷ 5 MΩ. Thus, if the feedback resistance R is chosen as $R \gg 104\ \text{mV}/I_0$ to ensure a negligible noise, (e.g. $R = 50$ KΩ for $I_0 = 10\ \mu$A), one has a typical bandwidth $B = 0.8 \div 1.5\ \text{MHz}/R$ (R in MΩ) (e.g., $B = 16 \div 30$ MHz), which is comparable with that intrinsic of the fibre, expecially for moderate signal amplitudes I_0.

In the basic configuration, the dynamic range and linearity of the polarimetric scheme are limited by the $S = \sin 2\Phi$ dependence. A simple correction of the type $S + S^3/6$ [20] gives a linearity error less than $\pm 0.14\%$ up to $2\Phi = 0.8$. A more efficient method, which ensures an unlimited dynamic range at the expense of some complexity, is to double the optical detector section with a second beamsplitter and photodiode receiver, orientated with an axis parallel to the input polarisation, so as to yield two signals $\tilde{I}_1$ and $\tilde{I}_2$ (cf. eqns. 8 and 9):

$$\tilde{I}_1 = I_0 \cos^2 \Phi \tag{8'}$$

$$\tilde{I}_2 = I_0 \sin^2 \Phi \tag{9'}$$

so that, with the same processing as S, the signal $\tilde{S} = \cos 2\Phi$ is obtained. From S and $\tilde{S}$, the angle Φ can be recovered with several methods. For example, as shown in Reference 17, the time derivatives of S and $\tilde{S}$ are first computed by analogue differentiation of the signals:

$$S' = 2\Phi' \cos 2\Phi \tag{14}$$

$$\tilde{S}' = -2\Phi' \sin 2\Phi$$

then, they are cross-multiplied to $\tilde{S}$ and $-S$, respectively, and the results are added to yield:

$$S'\tilde{S} - \tilde{S}'S = 2\Phi'(\cos^2 2\Phi + \sin^2 2\Phi) = 2\Phi'$$

and Φ' is finally integrated (with the penalty of DC component suppression if an analogue integration is employed) to obtain Φ [17].

A digital processing of S and $\tilde{S}$ may be used to preserve the DC component at the expenses of a discretisation error. In any case, the power splitting in two receivers, orientated at 0° and 45°, allows the extention of the dynamic range, and linearity of response to the limits attainable with electronic handling, at the expense of a 3 dB reduction of the signal I_0 in each channel. An all-fibre implementation of this approach is shown in Fig. 4. The wave leaving the coil is first split by an ordinary nonpolarising fibre coupler C, and by two polarising splitters BS with their axes orientated at 0° and 45° with respect to the zero-current polarisation, thus yielding the signal I_1, I_2, $\tilde{I}_1$ and $\tilde{I}_2$ at the photodetectors.

3.2 Interferometric readout

The nonreciprocal Faraday phaseshift 2Φ between orthogonal circularly polarised waves propagating in the same direction or, equivalently, between parallel polarised waves propagating in opposite directions, can in principle be read by a variety of interferometric configurations. However, to cancel the minute reciprocal birefringence that is residual in the fibre, the Sagnac interferometre is the mandatory choice. The measurement configuration based on this interferometre is well established, being that developed for inertial sensing of Sagnac phaseshift between counterpropagating waves, used in the fibre optic gyroscope [6, 23]. This configuration is readily adapted to current sensing [24], as shown in Fig. 6.

Two right (or left) handed circularly polarised waves are launched in opposite directions in the sensing coil by inserting quarter-wave retarders oriented at 45° with respect to the linear polariser P. After propagation, the two waves exhibit a relative phaseshift 2Φ and, because

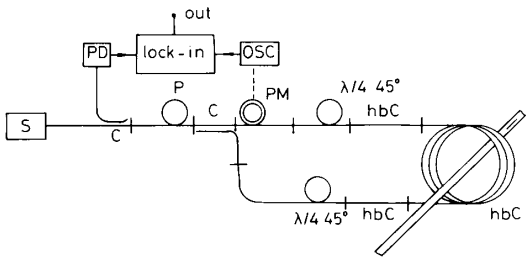

Fig. 6 *Interferometric readout*
P = polariser
C = couplers (nonpolarising)
$\lambda/4$ = quarter-wave retarders oriented at 45°
PM = phase modulator

of the folding in the winding, reappear at the quarter wave retarders as left (or right) handed circular polarisation. Thus, they are retransformed back to linear polarised waves, parallel to the launched one, and recombine on the photodetector yielding a beating signal $I_0(1 + \cos 2\Phi)$.

Other components in Fig. 6, as in the gyroscope, serve to ensure the reciprocity in splitting/recombining scheme (the two coupler C), to discriminate against spurious mode errors (the polariser P), and to impress a phase modulation PM [6, 23] which overcomes the difficulty of measuring Φ and its sign from the signal $\cos 2\Phi$.

If $\Phi_m \cos \omega_m t$ is the phase modulation asymmetrically impressed at time $t + \tau/2$ and $t - \tau/2$ on the two counterpropagating waves because of the coil propagating delay τ, the photodetected signal becomes:

$$I_s = I_0\{1 + \cos [2\Phi + \Phi_m \cos \omega_m(t + \tau/2) - \Phi_m \cos \omega_m(t - \tau/2)]\}$$

that, expanded in series of Bessel functions reads [23]:

$$I_s = I_0\{1/2 + 1/2J_0(\gamma\Phi_m) \cos 2\Phi + J_1(\gamma\Phi_m) \sin \omega_m t \sin 2\Phi + J_2(\gamma\Phi_m) \cos 2\omega_m t \cos 2\Phi + \ldots\} \tag{15}$$

where

$$\gamma = 2 \sin \omega_m \tau/2 \tag{16}$$

and $\tau = nL/c$ is the propagation time in the fibre of length L and refractive index n.

When $\gamma\Phi_m = 1.8$, the Bessel function J_1 reaches the maximum value:

$$J_1^m = 0.581$$

and therefore the component I_1 at the fundamental modulation frequency contained in I_s, measured, for example, with a lock-in amplifier (Fig. 6), is [6, 23]:

$$S = I_0 J_1^m \sin 2\Phi \tag{17}$$

which is the counterpart of eqn. 10. Also, one can recover, from the measurement of the second harmonic in I_s, the signal $\tilde{S} = I_0\ 0.32 \cos 2\Phi$ that is useful for linearity improvement and dynamic range extension.

The minimum detectable signal $\sigma(I)$ is determined by the shot noise associated with the photogenerated current I_0, and by the Johnson noise resistance of the receiver preamplifier, yet disregarding polarisation-

related errors. It is given by:

$$\sigma(I) = \sigma(S)/|\,dS/dI\,|$$

where $\sigma(S)$ as an expression similar to eqn. 11, and dS/dI is calculated from eqns. 3 and 17. Hence, we obtain, at the quantum-noise limit (i.e., for $R \gg 52\ \mathrm{mV}/I_0$ and $F = 1$):

$$\sigma(I) = (1/2J_1^{(m)}VN)(2eB/I_0)^{1/2} \tag{18}$$

A comparison with eqn. 12 shows that, in principle, interferometric and polarimetric readouts have nearly equivalent performances of minimum detectable current at the quantum-noise limit. The diagram of Fig. 5 can then be used, with the ordinates scaled by a factor $J_1^{(m)} = 0.581$, also for the interferometric readout.

It is worthwhile to note that, while the polarimetric scheme works in baseband and is therefore sensitive to slow fluctuations of the polarisation plane and of fibre birefringence besides $1/f$ noise, with a degradation of current sensitivity in DC, the interferometric readout works at the considerable high carrier frequency of the phase modulator, and its performance is as good in direct current as in AC.

The modulation frequency which yields the maximum phase deviation is, from eqn. 16:

$$f_m = 1/2\tau = c/4\pi nNr \tag{19}$$

or an odd multiple of this value.

Typically, $f_m = 3$ MHz for a $N = 50$ turns coil and $r = 10$ cm. In view of the amplitude-modulated structure of I_s with respect to the signals cos 2Φ and sin 2Φ that are impressed on the baseband ($\omega = 0$) and carrier frequency ($\omega = \omega_m$), respectively (eqn. 15), the maximum signal bandwidth is limited to $f_m/2$ (for $\Phi \ll 1$) to avoid spectrum overlap. Therefore, we have explicitly:

$$B = \mathrm{c}/8\pi nNr \tag{20}$$

which is about half the intrinsic bandwidth owing to the fibre structure (eqn. 13). However, the relatively high modulation frequency f_m of eqn. 19 may be difficult to achieve with the usual piezoceramic phase modulators. If a lower frequency is used, the maximum signal amplitude $J_1^{(m)}$ still be achieved, working with a larger phase deviation Φ_m (eqns. 15 and 16), but the bandwidth is then limited operatively to half the working frequency of the phase modulator.

As a concluding remark, from the analysis of theoretically achievable performances it turns out that polarimetric and interferometric readouts are substantially equivalent in terms of minimum detectable current, bandwidth and dynamic range or linearity. However, because of components limitations, the polarimetric scheme is more suitable for high bandwidth and high dynamic range, and the interferometric one more easily achieves high sensitivity, especially in DC measurements.

3.3 Closed-loop vs open-loop configurations

All the above considered readouts can be turned in a closed-loop configuration when a coil is wound on the fibre before entering in the photodetector section. The signal S is used to drive the coil with a current I_c so as to give a Faraday rotation equal and opposite to the measurand. Thus, S is kept zero by feedback, and the desired current is read as $I = nI_c$, n being the ratio of feedback coil turns to fibre coil turns [25, 26]. The closed-loop configuration can be implemented both in polarimetric and interferometric readout, and its advantages are the cancellation of nonlinearity errors due to the null measurement method, and the unlimited dynamic range, provided that the feedback loop is fast enough to follow the signal current. Obviously, noise is unchanged because at the input of the feedback loop and bandwidth is diminished to that of the feedback coil.

4 Fibres and birefringence control

In the previous Section, an ideal fibre was assumed to evaluate sensitivity performances, neglecting undesired birefringence effects which limit the maximum useful length of the sensing coil. Since the sensitivity $1/\sigma(I)$ or Φ/I of the current sensor is proportional to the product VN (eqns. 3 and 12 or 18), it is equally important to improve the material parameters by fabricating a special high-Vedet constant fibre as to increase the number of turns N by an appropriate geometry and a careful control of birefringence effects.

Special fibres may either be drawn from high-n Te-doped paramagnetic glasses, like FR-4 and FR-5 [27, 28] to exploit the dependence of V from n (eqn. 2), or from Y, Fe-doped ferromagnetic ion glasses which, close to the electronic transition ($\lambda \simeq \lambda_0$ in eqn. 2), yield a strongly enhanced Verdet constant, although keeping the attenuation coefficient reasonably low. A hundred fold increase of V with respect to silica fibres appears feasible using known materials (Fig. 1). However, if a special fibre is fabricated with poor control of residual birefringence, the improvement in V can be vanified by the decrease of useful length.

The maximum useful length L of fibre, and hence the maximum N, is limited by the linear birefringence β_l of the fibre to a value $L \ll 1/\beta_l$ if alteration of the ideal polarisation state is to be negligible. Both bend-induced birefringence and residual internal birefringence contribute to β_l, limiting L to a few decimetres in ordinary silica fibres. Moreover, since the compounding of linear and circular birefringence is quadratic (see below), when $\beta_l L \simeq 1$, the linear birefringence quenches the Faraday one. At the opposite, when a large circular birefringence $\beta_c \gg \beta_l$ is added to the fibre, for example by twisting it, the linear birefringence is quenched [20] and the Faraday component added to β_c is carried on unaltered.

4.1 Analysis of birefringence compounding

A quantitative analysis of the quenching effect is based on the standard Jones matrix method [2, 20], resulting in relatively lengthy calculations. In the following, we present a new derivation based on operator method.

Let us consider the propagation of the Jones vector $\underline{E} = [E_x, E_y]$ along the z-axis, and write the equation for an infinitesimal length dz as:

$$\underline{E}(z + dz) = \underline{J} \cdot \underline{E}(z) \tag{21}$$

where $\underline{J}$ is the Jones matrix. For the combined linear birefringence β_l and circular birefringence β_c (reciprocal) and $2HV$ (Faraday), the Jones matrix is [2, 29]:

$$\underline{J} = \underline{1} + \underline{M}\,dz \tag{22}$$

where $\underline{1}$ is the unity matrix, and $\underline{M}$ is given by:

$$\underline{M} = \begin{bmatrix} i\beta_l/2 & HV + \beta_c/2 \\ -HV - \beta_c/2 & -i\beta_l/2 \end{bmatrix} \tag{23}$$

Combining eqns. 22 and 21 yields the following differential equation for the propagation of the Jones vector $\underline{E}$:

$$d\underline{E}/dz = \underline{M} \cdot \underline{E} \tag{24}$$

The formal solution of eqn. 24 is:

$$\underline{E} = (\exp \underline{M}z) \cdot \underline{E}_0 \tag{25}$$

where $\exp \underline{M}z$ is an operator acting on the initial state vector $\underline{E}_0$ at $z = 0$. By developing eqn. 25 in power series, and noting that:

$$\underline{M}^{2n} = (-1)^n \Delta^{2n} \underline{1}, \quad \underline{M}^{2n+1} = (-1)^n \Delta^{2n} \underline{M},$$
$$n = 1, 2, \ldots$$

we have readily as a general solution:

$$\underline{E} = \cos \Delta z \underline{E}_0 + (1/\Delta) \sin \Delta z \underline{M} \cdot \underline{E}_0 \tag{26}$$

or, explicitly,

$$\underline{E} = \begin{bmatrix} \cos \Delta z + (1/\Delta) \sin \Delta z \; i\beta_l/2 & (1/\Delta) \sin \Delta z(HV + \beta_c/2) \\ (-1/\Delta) \sin \Delta z(HV + \beta_c/2) & \cos \Delta z - (1/\Delta) \sin \Delta z \; i\beta_l/2 \end{bmatrix} \tag{26'}$$

where Δ^2 is given by:

$$\Delta^2 = \beta_l^2/4 + (HV + \beta_c/2)^2 \tag{27}$$

This result coincides with that reported in Reference 19, and is confirmed by a direct analysis [30] based on Maxwell equations in the limit of ray optics approximation (β_c, β_l, $HV \ll 2\pi/\lambda$).

4.2 Birefringence quenching

Let us first consider a fibre without circular birefringence, i.e. $\beta_c = 0$. Since the terms determining the rotation in eqn. 26′ are periodic in Δz and the maximum rotation Φ is obtained for $\Delta z = \pi/2$, the useful fibre length is limited to $z = \pi/2\Delta$ or, if $\beta_l \gg 2HV$, to $z = \pi/\beta_l$ [20]. Under this condition it is $\underline{E} = (1/\Delta)\underline{M} \cdot \underline{E}_0$, i.e., the Faraday rotation contained in $\underline{M}$ is reduced by a factor $\Delta z = \pi/2$ respect to the expected value HVz. With a linear polarisation $\underline{E}_0 = [1 \quad 0]$ at the input, the propagating vector $\underline{E}(z)$ oscillates between linear and elliptical states of polarisation with a spatial period $z = 2\pi/\Delta$. The Faraday rotation term HVz is reduced by a factor $\sin \Delta z/\Delta z$, and vanishes for z multiple of π/β_l.

On the other hand, if we consider a fibre with uniformly distributed circular birefringence much larger than the linear birefringence, i.e. $\beta_c \gg \beta_l$, yet with a superimposed small Faraday birefringence $2HV \ll \beta_l$, the role of quenching is reversed, and the linear term $\beta_l z/2$ is reduced by a factor $\sin \Delta z/\Delta z$ while the linear polarisation rotates at a rate β_c.

More precisely, by developing Δ at the second order in $\rho = \beta_l/\beta_c$ and inserting in eqn. 26′ one finds:

$$\Delta = (HV + \beta_c/2)(1 + \rho^2/2)$$

$$\underline{E} = \begin{bmatrix} \cos \Delta z + i\rho(1 + \rho^2/2)^{-1} \sin \Delta z & \sin \Delta z(1 + \rho^2/2)^{-1} \\ -\sin \Delta z(1 + \rho^2/2)^{-1} & \cos \Delta z - i\rho(1 + \rho^2/2)^{-1} \sin \Delta z \end{bmatrix} \cdot \underline{E}_0$$

Let us express this matrix as the sum of a matrix of pure rotation $\Phi = \Delta z$, and of an elliptical birefringence matrix:

$$\begin{bmatrix} \cos \Delta z & \sin \Delta z \\ -\sin \Delta z & \cos \Delta z \end{bmatrix} + \rho(1 + \rho^2/2)^{-1} \sin \Delta z \begin{bmatrix} i & -\rho/2 \\ \rho/2 & -i \end{bmatrix}$$

The second term vanishes for z multiples of $\pi/\Delta \approx 2\pi/\beta_c$, i.e. for multiples of half the beating length of the circular birefringence. In any case, the error component is smaller than ρ in the relative field amplitude, and smaller than ρ^2 in the relative intensity of detected signals I_1 and I_2 (eqns. 8 and 9).

The quenching effect greatly reduces the effects of uniformly distributed linear birefringence, and hence increases the maximum useful fibre length. The limit now comes from the rare, randomly distributed spikes of linear birefringence owing, e.g., to fibre imperfections and microcurvatures that locally violate the condition $\beta_c \gg \beta_l$ and to eventual kinks and stresses imparted by coil former and downlead fixtures. With a careful control of fibre assembly, length in excess of 10 m can be achieved with negligible deterioration of the output polarisation state.

To implement birefringence quenching, one may use either a high circular birefringence fibre or a twisted spun fibre [20, 31, 37]. The former have been reported recently [32] to achieve beating length $L_b = 2\pi/\beta_b$ down to a few millimetres, and are the ideal choice for Faraday sensors, provided that a balanced configuration (see Section 4.3) is employed. The latter has the advantage of being readily available and of allowing adequate control of bending and internal residual linear birefringence in many cases.

For a twisted fibre, the circular birefringence induced by twisting is evaluated as [33–35]:

$$\beta_c = -2\pi n^2 p_{44}/\Lambda \tag{29}$$

where Λ is the twist period and p_{44} is an elasto-optic coefficient. Typical values for silica fibres are $\beta_c = 0.95 \div 1.05/\Lambda$. Bend-induced birefringence is the main contribution to linear birefringence of a coiled fibre, and is given [33] by the sum of pure bending birefringence β_{lb} and tension-induced birefringence β_{lt}:

$$\beta_l = \frac{2\pi}{\lambda} C_s \left[\frac{r^2}{2R^2} + \frac{2 - 3\nu}{1 - \nu} \frac{r}{R} S \right] = \beta_{lb} + \beta_{lt} \tag{30}$$

where C_s is a strain-optical coefficient:

$$C_s = (1/2)n^3(p_{11} - p_{12})(1 + \nu),$$

ν is the Poisson's modulus, r is the outer fibre radius and R is the coil radius. $S = F/(\pi r^2 E)$ is the axial strain produced by the tensile force F which stretches the fibre during coiling, and E is Young's modulus. Pure bending prevails on tension for $r/2R > S(2 - 3\nu)/(1 - \nu)$, which amounts for a typical silica fibre ($r = 50$ μm) to a tensile force of coiling $F < 0.8/R(N)$ for R in centimetres.

For silica fibres wound on small coil radius or with negligible tension, the value of β_{lb} is typically $0.2 \div 0.4/R^2$ (cm^{-1}), for R in centimetres. To quench the linear birefringence ($\beta_l \ll \beta_c$) in a spun fibre, it is twisted with a period $\Lambda \ll 2\lambda n^2 p_{44} R^2/C_s r^2$. This gives, for silica fibres with negligible tension, $\Lambda \ll 2.5 \div 5\, R^2$ (Λ and R in centimetres), i.e. a range of Λ from ~ 1 cm ($R = 2$ cm) to 25 cm ($R = 10$ cm) which is adequate for common current sensor geometries.

Stresses exerted by fixtures of fibre mountings and by unintentional kinks may add much larger localised birefringence. A fixture exerting a compressive force F on a fibre piece of length L gives a contribution [33, 34]:

$$\beta_{lf} = (8C_s/\lambda r E)F/L$$

which is reduced by a factor $(1 - \cos 2\delta \sin \delta)/2$ if the fibre is laid with friction on a V-groove of angle 2δ [33]. Then, the maximum F/L allowed by the condition $\beta_c \gg \beta_{lf}$ is:

$$F/L \ll \lambda \beta_c r E/8C_s$$

typically in the range $2 \div 3\beta_c(N/\text{cm})$, β_c (in cm^{-1}), or $2 \div 3/\Lambda$ (N/cm) for a fibre twisted with period Λ (cm). These figures indicate that fibre mounting and fastening can be designed without special problems.

The effect of kinks has been analysed in detail [36] and can be summarised as follows: a ridge of height H on a cylinder of radius R stretches the fibre for a length $(8HR)^{1/2}$ in which an excess birefringence is generated, of average value:

$$\beta_{1k} = \beta_{1b}(2HRS)^{1/2}/r$$

where β_{1b} is pure bending birefringence. The peak of excess birefringence is located over the kink and is considerably larger than β_{1k}. If we introduce two multiplication factors m_b and m_t of the terms given by eqn. 30 for pure bending β_{1b} and tension β_{1k}, the peak birefringence at the kink can be accounted for respect to the ideally smooth surface. From [36] these factors are calculated as:

$$m_b = 8HRS/r^2 \qquad m_t = (2HR)^{1/2}/r \tag{31}$$

Since the axial strain S is numerically small, one usually has $m_b \ll m_t$. For a kink lifting the fibre, H is not less than approximately the fibre diametre $2r$, and from eqn. 31, m_t is in the range $30 \div 60$ for $R = 2 \div 8$ cm, a value which may prevent quenching. However, if the fibre has a soft jacket and kinks on fibre are avoided, a moderate surface roughness is tolerable, since minute irregularities $H \ll r$ of the coil former are absorbed by the jacket.

4.3 Balanced configurations

When the circular birefringence $\Phi_c = \beta_c z$ bias is large, its temperature [20], stress and wavelength dependence may add an intolerable error in the measurement of the superimposed Faraday rotation Φ, especially in DC and at low frequences. The term Φ_c can, however, be cancelled with a balanced configuration: since Φ_c is a reciprocal rotation and Φ is nonreciprocal, by reversing the propagation from z to $-z$, Φ_c changes its sign and Φ is unchanged. Therefore, using a coil with a mirrored end and reading the return wave at the input end as in Fig. 7, the two-

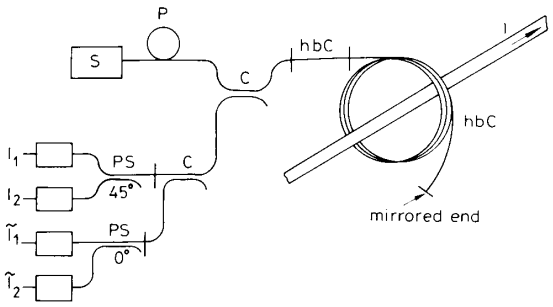

Fig. 7 *Balanced polarimetric readout* (cf. Fig. 4) *for cancelling reciprocal rotation* Φ_c *of the fibre*

waves rotations $\Phi + \Phi_c$ and $\Phi - \Phi_c$ add to 2Φ cancelling the reciprocal rotation. Thus, the polarimetric scheme can be balanced against common mode circular birefringence of the optical path, as it is the interferometric scheme of Fig. 6. The same arguments also apply to downlead fibre sections connecting source and detector to the sensing fibre, which give an error in an unbalanced scheme (Fig. 4) while are cancelled in balanced schemes (Fig. 6 and 7).

4.4 Other sources of errors

Several parasitic effects should be considered in a current sensor which can generate a large bias term Φ_b superimposed to the Faraday rotation Φ. The bias is an error in DC measurements and also affects the low-frequency sensitivity in AC measurements because of the spectral content associated with the slow fluctuations of Φ_b.

In polarimetric schemes, the angular error Φ_a of alignment of polariser axes respect to the 45° or 0° nominal values directly translates itself in a bias error, as it can be seen from eqns. 8, 9 or 8′, 9′ changing the argument by Φ_a.

Also, the finite extinction ratio of the polarisers can contribute a significant bias error. The upper limit of this error is $\Phi_b = \varepsilon a_B/a_A$, where a_B and a_A are the amplitudes of fields incident on the polariser perpendicular and parallel to the main axis and ε is the amplitude extinction factor of the polariser.

In the interferometric schemes, the error Φ_a in angular position of each quarter-wave retarder, and its deviation δ from the ideal $\pi/2$ phaseshift, give a bias error $\Phi_b = \Phi_a + \delta$, and the finite extinction of the polariser ε has the same effect found for the fibre gyro [23]: $\Phi_b = 2\varepsilon|a_B t_{AB}/a_A t_{AA}|$, where a_A and a_B are the amplitudes of the source light incident on the principal axes, and t_{AB} is the fraction of εa_B returned after propagation along the polariser axis A as an error superimposed to the useful wave $a_A t_{AA}$ [23].

Reflections at splices and couplers, and Rayleigh scattering in the fibre are sources of spurious interference for interferometric schemes, which can be overcome by using a source with low coherence length; in balanced polarimetric schemes, any reflection with amplitude coefficient r results in a maximum bias error $\Phi_b = r$. Mode conversion at joints between different fibres is another less severe source of error, which amounts to $\Phi_b = 2\eta|a_M t_{MN}/a_N t_{NN}|$ where η is the amplitude loss of mode conversion from N to M, a_M and a_N are the amplitudes of such modes contained in the launched light wave and t_{MN} is the fraction of ηa_M returned as useful mode distribution a_N.

5 Magnetic field sensors

Usually, magnetic flux measurements in electrical machinery require the smallest possible size of the sensing element, typically $R \sim 1$ cm, which is close to produce incipient bending attenuation [34]. Also, a different approach is needed in respect to the current sensor, since the Faraday rotation vanishes (eqn. 3′) for a closed loop unlinked to the current generating the magnetic field.

The combined effect of Faraday and linear birefringence gives a nonvanishing net result in a circular coil if the single turn is exactly a full-wave retarder [19, 29, 37], a condition for which $\beta_1 = 1/R$ or equivalently, the beat length matches the turn perimeter $L_b = 2\pi R$. Then, the output has the same state of polarisation as the input after one exact turn, and the Faraday effect gives the desired rotation Φ as in a straight fibre, but with half the expected value for the used fibre length [29, 31].

To have input and output fibres on the same side for ease of layout of the magnetic sensor, it is customary to employ an $N + 1/2$-turn coil (Fig. 8), for which the above considerations still apply [29]. In this geometry, for an input linearly polarised field E_{x0} normal to the coil plane, the output components E_y, E_x are:

$$E_x = -E_{x0} \cos \Phi_z \tag{32}$$

$$E_y = -E_{x0} \sin \Phi_z \tag{32'}$$

for a field H_z parallel to the input propagation vector (Fig. 8*a*), and

$$E_x = -E_{x0} \cos \Phi_y \tag{33}$$

$$E_y = -iE_{x0} \sin \Phi_y \tag{33'}$$

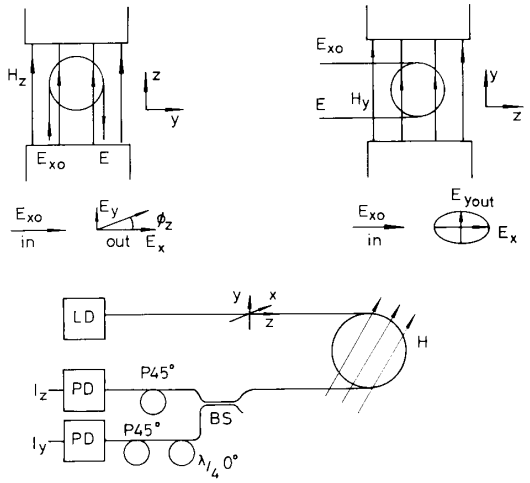

Fig. 8 *Magnetic field sensors based on λ-retarder per turn concept*
a gives a purely rotated linear-polarised output
b allows an easier allocation of the sensor and gives an elliptical output polarisation
c is the scheme for measuring both components H_z, H_y of the field

for a field H_y normal to the input propagation vector (Fig. 8*b*), where the Faraday angles $\Phi_{y,z}$ are:

$$\Phi_{y,z} = VH_{y,z}\pi R(N + 1/2) \tag{34}$$

As depicted in Fig. 8, in the first case, a pure Faraday rotation Φ_z is obtained, while in the second case, the output has an ellipticity Φ_y. For measurements in a gap with allowance for downlead trunks, Fig. 8*b* is a more suitable layout, and its output can be reconducted to purely rotated linear by adding a quarter-wave retarder.

Fig. 8*c* shows a polarimetric scheme for measuring simultaneously both H_z and H_y, thus allowing to compute the modulus $(H_y^2 + H_z^2)^{1/2}$ and the angle $\Psi = \tan^{-1} H_y/H_z$ of the magnetic field vector in the coil plane. A linear polarised wave is launched parallel to x – axis, and the output from the coil is splitted in two parts that are analysed in phase and in quadrature (upper and lower BS legs in Fig. 8*c*). The photodetected signals are therefore:

$$I_z = I_0 \cos^2 (45° + \Phi_z) \tag{35}$$

$$I_y = I_0 \cos^2 (45° + \Phi_y) \tag{36}$$

that are formally coincident with eqn. 8. Accordingly, the polarimetric readout concepts outlined in Section 3.1 can be applied to the measurement of H_y and H_z, as well as the extension of Fig. 4 for dynamic range and linearity improvement.

The performance evaluations of Section 3 are applicable to the magnetic sensor with the appropriate changes. As an example, the minimum detectable (or noise-equivalent) magnetic field is given by (cf. eqn. 12):

$$\sigma(H) = [1/2V(N + 1/2)\pi R](2eB/I_0)^{1/2} \tag{37}$$

Fig. 9 is a plot of eqn. 37 for silica fibres, and typical values of the parameters N and R. Also, each component Φ_z and Φ_y of the Faraday-induced rotation can be measured with the interferometric readout (see Fig. 6) to get a balanced configuration desensitised against downlead trunks.

In silica fibres, the typical radius R of λ-retarder per turn is, from eqn. 30, $R = 1/\beta_{lb} = 2 \div 4$ mm for untensioned fibres, and $R = 1/(\beta_{lb} + \beta_{lt}) = 4 \div 10$ mm for coil wound with a tension $F = 2 \div 5N$.

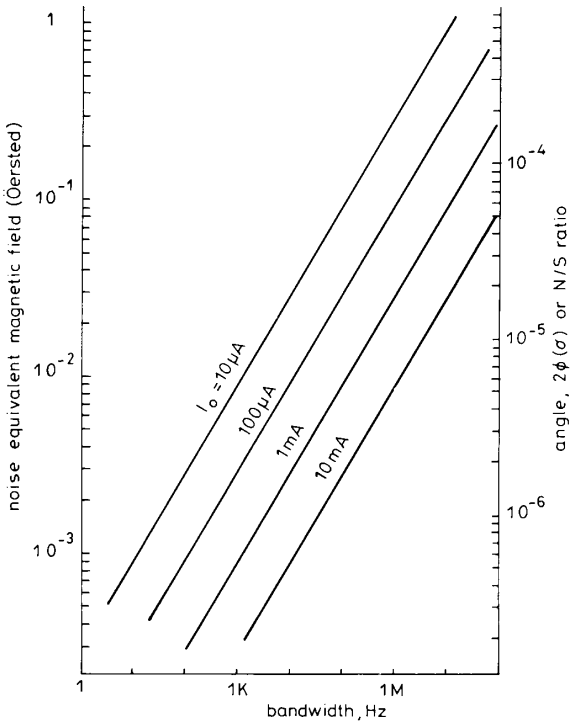

Fig. 9 *Noise equivalent magnetic field intensity H_0 against bandwidth B and detected current I_0*
Assumed parameters: $N = 50$; $V = 2.5$ μrad/A; $R = 1$ cm

5.1 Other geometries for mobile applications

When the physical dimensions of the sensor are not constrained, e.g. for measurements of flux external to electrical machinery, the quasistraight sensor configuration shown in Fig. 10 is well suited to increased L, and hence

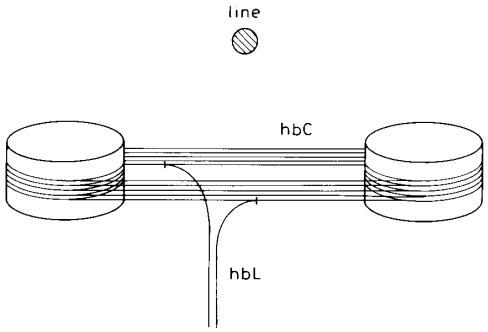

Fig. 10 *Quasi-straight magnetic field sensor*

sensitivity. The straight segments going back and forth are the field sensitive sections, and the curved edges serve to change Φ into $-\Phi$ at each reversal of the propagation vector, thus cumulating the opposite-sign Faraday rotation in the back and forth segments [38, 39]. The curved edges are half-wave retarders that give the sign reversal, made either by half turn ($R = 2 \div 4$ mm) or, to avoid small values, by one and a half turn ($R = 6 \div 12$ mm) [39]. An analysis of the Faraday rotation in a half wave

retarder of $n + 1/2$ turns gives zero as a result [29], and thus the total Faraday rotation Φ of the sensor is:

$$\Phi = VH2NL \tag{37}$$

where L is the length of segments. Using a low-birefringence spun fibre and trimming each half-wave edge during coil assembly, a relatively large effective length $2NL$ can be incorporated in the sensor [39]. Variants of the quasi-straight geometry are those of the fork [39] and of the broken ring [4].

Though these configurations are basically magnetic field sensors, they can be used in mobile application of current sensing because of the unlinked structure allowing to position the sensor around the line without disconnecting it. The broken ring, that is obtained by folding the quasi-straight structure on a helical single turn, offers a satisfactory insensitivity to position of the line inside the ring and a good immunity to external sources [4].

6 Experimental results

Data reported by several authors on current sensors performances (Table 1) indicate that the specifications required for power system applications (Section 1) can be substantially met. However, while linearity and dynamic range close to the predicted limits of performance (Section 3) have been obtained, the bandwidth capability is largely unexploited and usually traded-off to improve sensitivity. In fact, the less satisfactory performance in ordinary silica fibres is the minimum detectable signal, and moreover the obtained results are far from the quantum noise limit, as can be seen in Fig. 5. Here we draw segments joining experimental points and corresponding theoretical points at the quantum noise limit, after a standardisation of all data to $N = 50$ for comparison. In Fig. 5, the results plotted are, from left to right, those of References 2, 26, 2, 4 and 20, the last being for the noise of the electronics only. Other results of Table 1, not shown because incomplete, would exhibit even larger differences if the missing parameters are conservatively estimated.

To assess the relative importance of the sensor subsystems in the degradation of sensitivity, we measured the noise spectral density $\Gamma_I(f)(A/\sqrt{Hz})$ of the total noise equivalent current σ_I, explicitly given by $\sigma_I^2 = \int_0^B \Gamma_I^2(f)\, df$, for a typical polarimetric unbalanced configuration. The sensor has $N = 50$ fibre turns of twisted spun fibre (York LB 800) wound on a 8 cm diameter coil, and the source is a GaAlAs multimode laser (Telefunken TXAD 8100) supplying a detected current $I_0 = 100\ \mu$A at the preamplifier, the bandwidth of which is 500 kHz. The measurements were performed with a spectrum analyser at the electronics output. $\Gamma_I(f)$ was computed by dividing these readings by the responsivity of the sensor. Starting from the bare electronics and adding components up to the complete sensor yielded the results reported in Fig. 11. Curve *a* is for the noise of the electronics, with photodiodes at dark ($I_0 = 0$) and corresponds to a noise floor of 0.02 mA/$\sqrt{\text{Hz}}$.

Feeding a shot-noise limited current $I_0 = 100\ \mu$A through an external generator resulted in the expected noise floor of 0.23 mA/$\sqrt{\text{Hz}}$ (curve b). Curve c is for the same current $I_0 = 100\ \mu$A, but actually photodetected using the laser as the source. Thus, the ratio of the curves *c* and *b* represents the excess noise F due to the source. By inserting the polariser/analyser section, the noise did not appreciably increase. When the fibre was finally added, curves typically laying in between *d* and *e* were observed, the level of noise being correlated to external mechanical and thermal perturbations. The lower curve *e* is representative of a mechanically assembled sensor on a stable, but not isolated, table in the laboratory

Table 1: Summary of reported results

Configuration[a]	Open (0) or closed (*c*) loop	λ, nm	Number of turns, N	Twist rate, r/m	Coil diameter cm	Central frequency, Hz	Bandwidth, Hz	Detected power, mW	Reported $\sigma(I)$, A	$\sigma(I)$ reduced to $N = 50$, A	Dynamic range	Linearity error, %	Temperature range, °C	% error in temperature range or zero drift, A/°C	Reference
P	0	633	20	—	15	85	130 3 K	0.5	55 m 0.25	22 m 0.10	1.2 KA	0.24	−18 +45	±0.5	2
P	0	633	56	120	6		100 K	1	0.1[c]		1.8 KA	0.14		80	20
P	0	820	15	—	15		10 K	0.2	1	0.3	1 KA	<1			4
P	*C*	790	4200[b]	120	—	280			0.5 m	0.042					26
P	0	830	53 × 800[b]	120	24				3 m	2.4	90 dB				39
P	*C*	830	53 × 800[b]	120	24										25
I	0	780	45 × 580[b]	120	30	50			10 m	5.3	>40 dB				24

[a] *P* = polarimetric, *I* = interferometric; [b] = current conductor turns; [c] = noise of electronics

environment. By careful decoupling of the sensor from ambient through a proper enclosure, curve f was obtained. This is close to the quantum noise limit of performance.

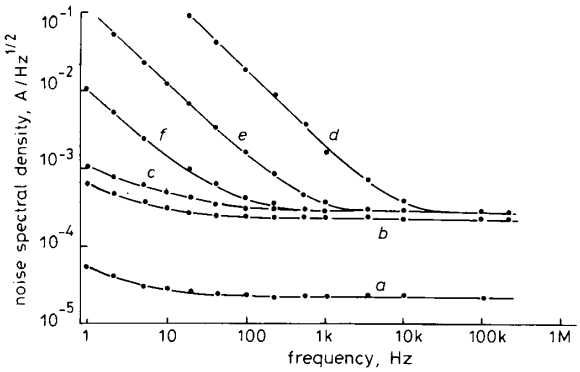

Fig. 11 *Contributions to the noise spectral density $\Gamma_I(f)$ of the measurand current I*

7 Conclusion

At present, current sensors can meet the performance specifications for application in electrical industry. However, further engineering efforts should be devoted to fibres and configurations least sensitive to vibrations and thermal perturbations, such as high elliptical or circular birefringence fibres and balanced or actively compensated configurations [41].

8 Acknowledgment

This work was performed under an MPI 40% contract.

9 References

1 RZEWUSKI, M.N., and TARNAWECKY, M.Z.: 'Unconventional methods of current detection and measurement in EHV and UHV transmission systems', *IEEE Trans. Inst. and Meas.*, 1975, **IM-24**, pp. 43–51

2 PAPP, A., and HARMS, H.: 'Magneto-optical current transformers', *Appl. Opt.*, 1980, **19**, pp. 3729–3745

3 YOSHINO, T.: 'Optical fiber sensors for the electrical industry', *Proc. SPIE symposium on Fiber Optic Sensors II*, 1987, **798**, pp. 258–265

4 ANNOVAZZI LODI, V., and DONATI, S.: 'Fiber current sensors for HV lines', *ibid.*, 1987, **798**, pp. 270–274

5 KURODA, Y., ABE, Y., KUWAHARA, H., and YOSHINAGA, K.: 'Field test of fiber optic voltage and current sensors applied to gas insulated substations', *ibid.*, 1985, **586**, pp. 30–37

6 GIALLORENZI, T.G., BUCARO, J., DANDRIDGE, A., SIEGEL, G., COLE, J.H., RASHLEIGH, S.C., and PRIEST, R.G.: 'Optical fiber sensor technology', *J. Quantum. Elect.*, 1982, **QE-18**, pp. 626–665

7 PITT, G.D., EXTANCE, P., NEAT, R.C., BATCHELDER, D.N., JONES, R.E., BARNETT, J.A., and PRATT, R.H.: 'Optical-fibre sensors', *IEE Proc.*, Pt. J, 1985, **132**, pp. 214–248

8 FREISER, M.J.: 'Survey of magneto-optic effects', *IEEE Trans. Magn.*, 1968, **MAG-4**, pp. 152–161

9 VOIGT, W.: 'Magneto-und Elektro-Optik' (Teubner Publishing, Leipzig 1908)

10 TABOR, W.J.: 'Magneto-optic materials', in 'Laser handbook', vol. 1, (Arecchi and Schultz du Bois (eds), North Holland, 1972, pp. 1011–1127)

11 PERSHAN, P.S.: 'Magneto-optical effects', *J. Appl. Phys.*, 1967, **38**, pp. 1482–1490

12 ROSSI, B.: 'Optics'. (Addison-Wesley Co., 1965)

13 PISAREV, R.V., SINII, I., and SMOLENSKI, G.: 'Rotation of polarisation plane and magnetic circular dichroism in $RbNiF_3$', *Sov. Phys., Solid State*, 1968, **9**, pp. 2482–2488

14 DANDRIDGE, A., TVETEN, A.B., and GIALLORENZI, T.G.: 'Interferometric current sensors using optical fibers', *Electron. Lett.*, 1981, **17**, pp. 523–525

15 PALIK, E.D. (ed.): 'Handbook of optical constants' (Academic Press, 1985.)

16 POOLE, S.B., PAYNE, D.N., and FERMANN, M.E.: 'Fabrication of low-loss optical fibers containing rare-earth ions', *Electron. Lett.*, 1985, **21**, pp. 737–738

17 DONATI, S.: 'Interferometry by induced modulation of cavity field', *J. Appl. Phys.*, 1978, **49**, pp. 495–498

18 SARID, D., DEETER, M.N., and KAHWATY, V.: 'Optical probing of magnetic inert layers', *Appl. Opt.*, 1987, **26**, pp. 3153–3157

19 SMITH, A.M.: 'Polarization and magneto-optic properties of single mode optical fiber', *ibid.*, 1978, **17**, pp. 52–57

20 RASHLEIGH, S.C., and ULRICH, R.: 'Magneto-optic current sensing with birefringent fibers', *Appl. Phys. Lett.*, 1979, **34**, pp. 768–770

21 MUOI, T.V.: 'Receiver design for high speed optical fiber systems', *IEEE J. Lightw. Tech.*, 1984, **LT-2**, pp. 243–267

22 THOMPSON, G.H.B.: 'Physics of Semiconductor laser devices' (J. Wiley & Sons, 1980.)

23. BERGH, R.A., LEFEVRE, H.C., and SHAW, H.J.: 'An overview of fiber-optic gyroscopes', *J. Lightw. Tech.*, 1984, **LT-2**, pp. 91–107

24 LEILABADY, P.A., WAYTE, A.P., BERWICK, M., JONES, J.D.C., and JACKSON, D.A.: 'A pseudo reciprocal fiber optic faraday rotation sensor: current measurement and data communication applications', *Optics Comm.*, 1986, **59**, pp. 173–176

25 KERSEY, A.D., and DANDRIDGE, A.: 'Optical fibre faraday rotation current sensor with closed loop operation', *Electron. Lett.*, 1985, **21**, pp. 464–465

26 BERWICK, M., JONES, J.D.C., and JACKSON, D.A.: 'Alternating current measurement and noninvasive data ring utilizing the faraday effect in a closed-loop magnetometer', *Optics Lett.*, 1987, **12**, pp. 293–295

27 SHIRAISHI, K., NISHINO, K., and KAWAKAMI, S.: 'Temperature insensitive fiber faraday rotator', *Appl. Opt.*, 1985, **24**, pp. 1896–1897

28 KOBAYASHI, K., and SEKI, M.: 'Micro-optic grating multiplexers and optical isolators for fiber optics communications', *IEEE J. Quant. Electron.*, 1980, **QE-16**, pp. 11–22

29 ANNOVAZZI LODI, V., and DONATI, S.: 'Combined reciprocal and nonreciprocal birefringence in optical monomode fibers', *J. Opt. and Quantum Electron.*, 1983, **15**, pp. 381–388

30 TABOR, W.J., and CHEN, F.S.: 'Electromagnetic propagation through materials possessing both faraday rotation and birefringence: experiments with ytterbium orthoferrite', *J. Appl. Phys.*, 1969, **40**, pp. 2760–2765

31 DAY, G.W., PAYNE, D.N., BARLOW, A.J., and RAMSKOV-HANSEN, J.J.: 'Faraday rotation in coiled monomode optical fibers: isolators, filters and magnetic sensors', *Opt. Lett.*, 1982, **7**, pp. 238–241

32 HUSSEY, C.D., BIRCH, R.D., and FUJI, Y.: 'Circularly birefringent single-mode optical fibers', *Electron. Lett.*, 1986, **22**, pp. 129–130

33 RASHLEIGH, S.C.: 'Origins and control of polarization effects in single-mode fibers', *J. Lightwave Technol.*, 1983, **LT-1**, pp. 312–331

34 ANNOVAZZI LODI, V., and DONATI, S.: 'Stressed optical fibers and their use as polarizing components', *Alta Freq.*, 1982, **51**, pp. 159–163

35 ULRICH, R., RASHLEIGH, S.C., and EICHOFF, W.: 'Bending induced birefringence in single-mode fibers', *Optics Lett.*, 1980, **5**, pp. 273–275

36 ULRICH, R., and RASHLEIGH, S.C.: 'Polarization coupling in kinked single-mode fibers', *IEEE J. Quantum. Electron.*, 1982, **QE-18**, pp. 2032–2039

37 PAYNE, D.N., BARLOW, A.J., and RAMSKOV HANSEN, J.J.: 'Development of low and high birefringence optical fibers', *ibid.*, 1982, **QE-18**, pp. 477–487

38 BERGH, R.A., LEFEVRE, H.C., and SHAW, H.J.: 'Geometrical fiber configuration for isolators and magnetometers', in 'Fiber-optic rotation sensors', (S. Ezekiel and H.J. Arditty (Eds), Springer Verlag, 1982, pp. 400–405)

39 DONATI, S., and ANNOVAZZI LODI, V.: 'Fiber sensor for current measurements in power lines', *Alta Freq.*, 1984, **53**, pp. 310–314

40 KERSEY, A.D., and JACKSON, D.A.: 'Current sensing utilizing heterodyne detection of the faraday effect in single-mode optical fiber', *J. Lightwave Technol.*, 1986, **LT-4**, pp. 640–643

41 LAMING, R.I., PAYNE, D.N., and LI, L.: 'Current monitor using elliptical birefringent fibre and active temperature compensation', *Proc. SPIE Symposium on Fiber Optic Sensors II*, 1987, **798**, pp. 283–287